Thickness-dependent polarization-induced intrinsic magnetoelectric effects in La_{0.67}Sr_{0.33}MnO_{3}/PbZr_{0.52}Ti_{0.48}O_{3} heterostructures

Xiaoqian Yu, Lijun Wu, Bangmin Zhang, Hua Zhou, Yongqi Dong, Xiaohan Wu, Ronghui Kou, Ping Yang, Jingsheng Chen, Cheng-Jun Sun, Yimei Zhu, and Gan Moog Chow

Phys. Rev. B **100**, 104405 — Published 3 September 2019

DOI: 10.1103/PhysRevB.100.104405

Thickness-dependent polarization-induced intrinsic magnetoelectric effects in $La_{0.67}Sr_{0.33}MnO_3/PbZr_{0.52}Ti_{0.48}O_3$ heterostructures

Xiaoqian Yu[1], Lijun Wu[2], Bangmin Zhang[1,3], Hua Zhou[4], Yongqi Dong[4], Xiaohan Wu[1], Ronghui Kou[4], Ping Yang[5], Jingsheng Chen[1], Cheng-Jun Sun[4,*], Yimei Zhu[2,*], and Gan Moog Chow[1,*]

[1]*Department of Materials Science & Engineering, National University of Singapore, 117576, Singapore.*

[2]*Condensed Matter Physics & Materials Science Division, Brookhaven National Laboratory, New York 11973, USA.*

[3]*Department of Physics, Sun Yat-Sen University, Guangzhou, 510275, PRC*

[4]*Advanced Photon Source, Argonne National Laboratory, Argonne, Illinois 60439, USA*

[5]*Singapore Synchrotron Light Source, National University of Singapore, 117603, Singapore*

**Corresponding Authors' Email: cjsun@aps.anl.gov; zhu@bnl.gov; msecgm@nus.edu.sg.*

ABSTRACT

The polarization of $PbZr_{0.52}Ti_{0.48}O_3$ thin film is switched by changing film thickness through the competition between the strain relaxation-induced flexoelectric fields and the interfacial effects. Without an applied electric field, this reversal of polarization is exploited to control the magnetic properties of $La_{0.67}Sr_{0.33}MnO_3$ by the competition/cooperation between the charge-mediated and the strain-mediated effects. Scanning transmission electron microscopy, polarized near edge x-ray absorption spectroscopy, and half-integer diffraction measurements are employed to decode this intrinsic magnetoelectric effects in the $La_{0.67}Sr_{0.33}MnO_3/PbZr_{0.52}Ti_{0.48}O_3$ heterostructures. With $PbZr_{0.52}Ti_{0.48}O_3$ films < 48 nm, the polarization-driven carrier density modulation around the $La_{0.67}Sr_{0.33}MnO_3/PbZr_{0.52}Ti_{0.48}O_3$ interface and the strain-mediated Mn 3*d* orbital occupancy work together to enhance the magnetism of 14 unit cells $La_{0.67}Sr_{0.33}MnO_3$ film; with $PbZr_{0.52}Ti_{0.48}O_3$ layers > 48 nm, the strain-induced change of bond length/angle of MnO_6 accompanied with a modified spin configuration are responsible for the decrease in Curie temperature and magnetization of 14 unit cells $La_{0.67}Sr_{0.33}MnO_3$ film.

I. INTRODUCTION

Artificially designed multiferroic heterostructures of ferromagnetic (FM) /ferroelectric (FE) layers draw significant interests due to the rich physics of magnetoelectric (ME) coupling and potential applications [1-6]. Specially, the reversal of FE polarizaton by electric fields in multiferroics is of particular interest because of reduced power consumption [7]. For example, reversal of FE polarization-induced electrostatic modulation in the charge carrier density at the $La_{0.8}Sr_{0.2}MnO_3/PbZr_{0.2}Ti_{0.8}O_3$ interface [8, 9], or interfacial orbital reconstruction in $La_{0.5}Sr_{0.5}MnO_3/BaTiO_3$ [10] and $La_{0.825}Sr_{0.175}MnO_3/PbZr_{0.2}Ti_{0.8}O_3$ [11] have been reported. Most studies focus on the FM/FE interface with limited work on the effect of the FE film thickness. Previous work demonstrated the thickness dependence of interfacial coupling in $SrTiO_3$ (STO)/$Pr_{0.67}Sr_{0.33}MnO_3$ (PSMO) heterostructures [12], i.e. with an increase of PSMO thickness, magnetic properties around the STO/PSMO interface were modified due to the change of interfacial coupling of crystal structures. Considering the similarity between the FM and the FE materials of 3*d* transition-metal oxides, the structural and ferroelectric properties around the FM/FE interface may be modulated by the FE film thickness, which may be exploited to study the intrinsic ME effects in FM/FE heterostructures without an external electric field.

With increasing FE thickness, the direction of polarization may be manipulated by the flexoelectric effects through strain relaxation [13], leading to the change of interfacial charge screening in the FM thin film layer. At the same time, the strain effects, accompanied with increasing FE thickness, also influence the FM layer and modulate its crystal structure and electronic structure through lattice mismatch, octahedral connectivity, atomic displacement and orbital hybridization [12, 14, 15]. The competition/cooperation of the charge-mediated [16, 17] and strain-mediated [18, 19] effects stands out, yielding a robust ME response through the change of the crystal structure and chemical valences [14,

20]. In order to have a better understanding of this entangled interaction, an in-depth investigation on the ME coupling mechanisms in the FM/FE heterostructures is much warranted.

In this work, we report an integrated study on the intrinsic ME coupling in (001) $SrTiO_3$ (STO)/$La_{0.67}Sr_{0.33}MnO_3$ (LSMO, fixed at ~14 unit cells) /$PbZr_{0.52}Ti_{0.48}O_3$ (PZT, 0-130 nm) heterostructures without an applied electric field. $La_{1-x}Sr_xMnO_3$, as a metallic bottom electrode, may be used to induce the self-poling of $PbZr_{1-x}Ti_xO_3$ thin film [21], which points downward to the substrate in this study. By increasing the PZT thickness, switching of polarization direction is realized through the competition between the interfacial effects and the strain relaxation-induced flexoelectric fields, resulting in noticeable effects on the ME coupling in the LSMO/PZT heterostructures. Thin PZT films (< 48 nm) drive the holes depletion at the LSMO/PZT interface and the preferential Mn 3*d* out-of-plane orbital occupancy, enhancing magnetism of 14 unit cells LSMO film. The strain-induced modifications of bond length/angle of MnO_6 associated with a modified magnetic spin configuration decrease the Curie temperature and magnetization of 14 unit cells LSMO film with thick PZT films (> 48 nm).

II. EXPERIMENTAL

LSMO/PZT bilayered thin film heterostructures were fabricated by pulsed laser deposition (PLD) on the (001) STO single crystal substrates. LSMO thin film was deposited at 750°C under background oxygen pressure of 200 mTorr. PZT thin film was grown on the top of LSMO at 550 °C under 50 mTorr oxygen pressure. The laser fluence was kept at 1~2 J/cm^2 and the pulse repetition frequency was 3 Hz. After the deposition, the sample was cooled down to room temperature at 15°C/min in a 1 Torr oxygen atmosphere. The thickness of LSMO was fixed at ~14 unit cells (u.c.), which was determined by considering both the dead layer thickness and interfacial charge screening length. It is known that

metallic $La_{1-x}Sr_xMnO_3$ has a carrier density of 10^{21}-10^{22}/cm^3, yielding a screening length of less than 1 nm [22]. The presence of magnetically dead layer is well known for manganite perovskite and the thickness is found to be around 2 to 5 nm depending on the substrates [23]. Thus, LSMO of ~14 u.c. was chosen to reduce the impact of dead layer and to enhance the interface-to-volume ratio. $PbZr_{0.52}Ti_{0.48}O_3$ (PZT) is a good ferroelectric candidate in FM/FE heterostructures due to its high remanent polarization and outstanding piezoelectric coefficient [24]. The structural and ferroelectric properties of PZT depend on the film thickness, which was chosen as 4, 8, 16, 48, 96 and 130 nm.

Magnetic properties were measured by a superconducting quantum interference device (SQUID) and x-ray magnetic circular dichroism (XMCD), using beamline 4-ID-C of Advanced Photon Source (APS), Argonne National Laboratory, USA. Piezoresponse force microscopy (PFM) was used to measure the spontaneous polarization of as-grown PZT thin films. Crystal structure was determined by high-resolution x-ray diffraction using synchrotron x-ray sources at the x-ray development and demonstration (XDD) beamline of Singapore Synchrotron Light Source (SSLS) and beamline 12-ID-D of APS, Argonne National Laboratory, USA. Room temperature x-ray absorption near edge spectroscopy (XANES) measurement was performed using linear polarized x-ray at beamline 20-ID-B of the APS, Argonne National Laboratory, USA. Total fluorescent yield (TFY) was detected and the XANES normalization was conducted using the program Athena. High-angle annular dark field (HAADF) and annular bright field (ABF) in scanning transmission electron microscopy (STEM) and electron energy loss spectroscopy (EELS) were performed using the double aberration-corrected JEOL-ARM200CF microscope with a cold-field emission gun and operated at 200 kV, at Brookhaven National Laboratory, USA. The microscope is equipped with JEOL and Gatan HAADF detectors for

incoherent HAADF (Z-contrast) imaging, Gatan GIF Quantum ER Energy Filter with dualEELS for EELS.

III. RESULTS AND DISCUSSION

A. Modulation of LSMO properties by PZT thickness

$La_{0.67}Sr_{0.33}MnO_3$ (LSMO) is chosen as a ferromagnetic component in the multiferroic heterostructure due to its good half-metallic behavior with high Curie temperature and high spin polarization [25], which are sensitive to external stimuli. As shown in Figures 1a-1b, the Curie temperature T_c and the saturation magnetization M_s vary coherently with increasing PZT thickness. T_c was determined by finding the temperature for which the first derivative of the temperature-dependent magnetization curve has a minimum value (the inset of Figure 1a), while M_s was acquired by the maximum magnetization under the 10 kOe magnetic field (Figure 1b). As summarized in Figure 1c, in comparison with the pure LSMO (i.e. 0 nm PZT), the magnetic properties of LSMO are first enhanced and then suppressed with increasing PZT thickness. It is noted that the magnetic properties are linked to the Mn sites in LSMO, since only negligible contributions from Ti are found, as shown in Ti XMCD of Figure S1 in the Supplemental Material (SM) [26]. The measurement of magnetic hysteresis loops at 120 K is shown in Figure S2 of SM. The variation of M_s as a function of PZT thickness at 120 K is found to be consistent with that measured at 10 K, which indicates that the change of magnetism is not due to the STO phase transition at ~ 105 K.

The variation of electrical properties of LSMO with increasing PZT thickness is in accordance with the changing trend of magnetism. In Figure 1d, metal-insulator transition temperature T_{MI} is decreased by 25 K from the largest value (~ 309 K) to the smallest (~ 284 K) with increasing PZT thickness. The

details of the change of T_{MI} as a function of PZT thickness are summarized in Table I. The origin of above observed results will be discussed below.

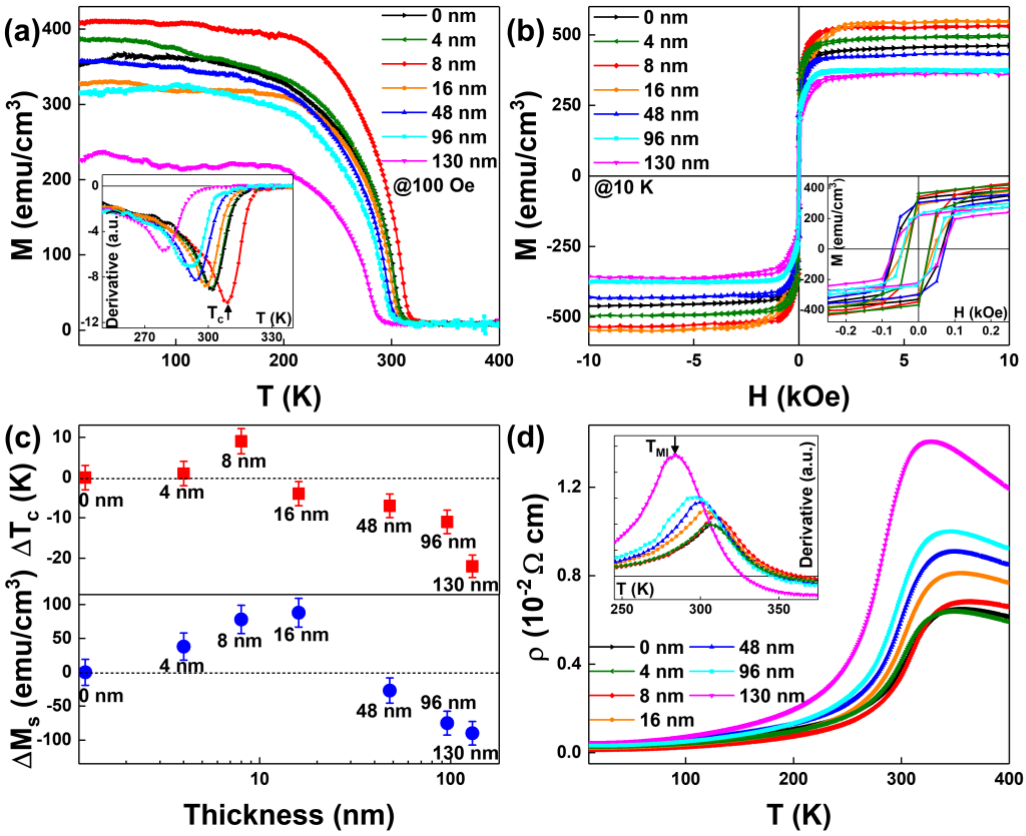

Figure 1. (a) Magnetization versus temperature (M-T) curves for LSMO with different thicknesses of PZT under an applied 100 Oe magnetic field. The inset shows the first derivative of the M-T curve with a minimum value that is defined as Curie temperature T_c. (b) Magnetic hysteresis loops of LSMO with different thicknesses of PZT measured at 10 K with an applied 10 kOe magnetic field. The inset shows the enlarged part of the magnetic hysteresis loops at low field ranges. (c) Summary of the T_c difference (ΔT_c) and the M_s difference (ΔM_s) between the pure LSMO with 0 nm PZT and the LSMO with increasing thickness of PZT. (d) Resistivity versus temperature (R-T) curves for LSMO with different thicknesses of PZT without an applied magnetic field. The inset shows the first derivative of the R-T curves with a maximum value that is defined as metal-insulator transition temperature T_{MI}.

Table I: T_{MI} of LSMO films as a function of PZT thickness.

PZT thickness (nm)	0	4	8	16	48	96	130
T_{MI} (K)	306 (± 3.06)	305 (± 3.05)	309 (± 3.09)	303 (± 3.03)	300 (± 3.00)	296 (± 2.96)	284 (± 2.84)

B. Thickness-dependent crystal structures of PZT films

The properties of manganite are strongly correlated with crystal structures. The LSMO/PZT heterostructures were investigated using reciprocal space mappings (RSM). As shown in Figures 2a-2c, all the LSMO thin films are completely strained on the STO substrate, inferred from the vertical alignment of reciprocal lattice points of LSMO and STO. Thus, the in-plane lattice constants of LSMO are the same as those of substrate. The tetragonal structure is determined by the same L values in all {103} mappings of LSMO in three samples [27], as shown in Figures S3a-S3c of SM. In Figures 2d-2f, the vertical displacement of PZT reciprocal lattice points from those of STO demonstrates that all PZT thin films are relaxed. This is possibly due to the misfit dislocations at interface and oxygen vacancies in PZT films. Based on the RSMs in Figures S3a-S3c, the calculated in-plane lattice constants are a=b=4.078 Å, 4.068 Å, 4.047 Å, and the out-of-plane lattice constants are 4.125 Å, 4.114 Å, and 4.079 Å, for 130 nm, 48 nm, and 8 nm PZT, respectively. More detailed information on the lattice parameters of LSMO/PZT is found in Figure S4 of SM [28-30] (see also [1-3] therein).

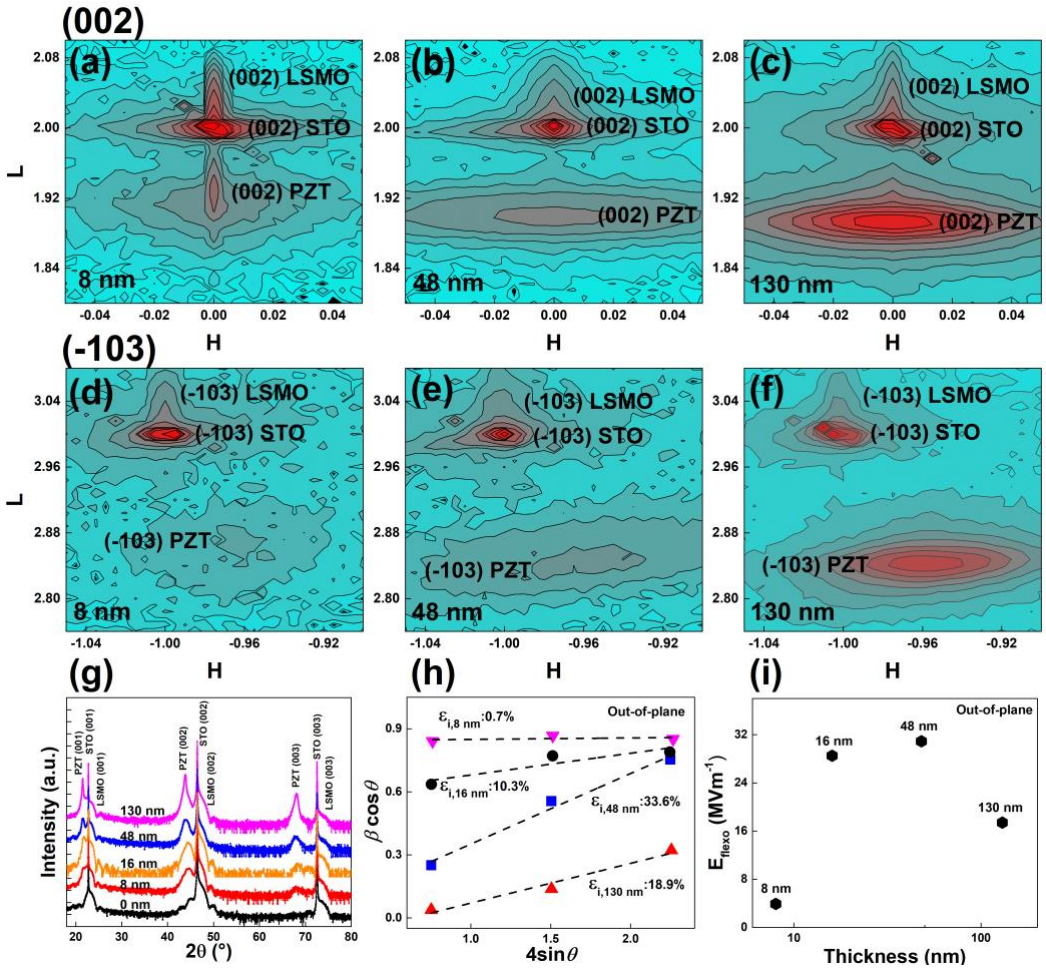

Figure 2. Reciprocal space mappings (RSMs) around (a)-(c) (002) and (d)-(f) (-103) of STO/LSMO (~14 u.c.) with 8 nm, 48 nm, and 130 nm PZT, respectively. (g) XRD θ-2θ scans for STO/LSMO (~14 u.c.) with different thicknesses of PZT thin films. (h) The out-of-plane Williamson-Hall plots for the inhomogeneous strain (ε_i) of the PZT films. (i) The out-of-plane flexoelectric fields as a function of PZT thickness.

Considering the lattice parameters of bulk tetragonal $PbZr_{0.52}Ti_{0.48}O_3$ ($a_{tetragonal}$ = 4.046 Å, $c_{tetragonal}$ = 4.139 Å), the coexistence of tetragonal and rhombohedral phase is proposed in PZT films [31, 32]. The relative weight of rhombohedral and tetragonal structure is found to be varied with film thickness. The dominant tetragonal structure is indicated by the same L values in all {103} mappings of 130 nm and 48 nm PZT films, as shown in Figures S3a-S3b. A small difference in L values of (013) and (0-13) can be seen in 8 nm PZT (Figure S3c), where L=2.872 for PZT (013) and L=2.856 for PZT (0-13), suggesting a non-90° angle between direct lattice constant b and c. Similarly, a minor difference in L

values of PZT (103) and PZT (-103), where L=2.864 for PZT (103) and L=2.872 for PZT (-103), indicates a non-90° between the direct lattice constants a and c. Hence, a dominant weight of rhombohedral phase is suggested in the 8 nm PZT.

In order to obtain more quantitative information, the strain gradients were estimated using the Williamson-Hall (W-H) plots [33]. The W-H plots of PZT thin film were obtained from XRD θ-2θ peak widths. In Figure 2g, three peaks (001), (002) and (003) from θ-2θ scans were used to determine the out-of-plane change of strain status in PZT. According to previous studies [34], the strain gradient is derived from inhomogeneous strain, ε_i, which could be determined from the slope of the fitted equation (the dash line). As shown in Figure 2h, β corresponds to the peak width, mainly contributed from the inhomogeneous strain ε_i and finite thickness of samples. The ε_i, values are determined as 0.7%, 10.3%, 33.6% and 18.9% for 8 nm, 16 nm, 48 nm and 130 nm PZT, respectively. From the inhomogeneous strain values and the assumption of strain penetration length, we estimated the out-of-plane strain gradients as -8.7×10^5 m^{-1}, -6.4×10^6 m^{-1}, -7.0×10^6 m^{-1} and -3.9×10^6 m^{-1}, accordingly. Based on the reported equation [35], the flexoelectric field (E_{flexo}) values were determined as 3.9 MVm^{-1}, 28.5 MVm^{-1}, 30.9 MVm^{-1} and 17.4 MVm^{-1}, respectively, as shown in Figure 2i. The calculated values are larger than the published data in previous reports [36]. We note that the presence of secondary phase and defects such as oxygen vacancies in PZT thin film may contribute to the peak broadening, thus increasing the ε_i and strain gradient. The effect of such high E_{flexo} on ferroelectric properties is discussed as below.

C. Reversal of polarization of self-poled PZT films

The direction of polarization in FE films depends on film thickness and strain relaxation. The strain gradient-mediated flexoelectric effect may affect the polarization of self-poled PZT. As shown in Figures 3a-3c, the typical out-of-

plane PFM poling and imaging [37, 38] were performed to probe the polarization direction of PZT as a function of its film thickness. The negative-voltage poled region corresponds to polarization pointing away from the substrate (P_{up}) while the positive-voltage poled region stands for polarization pointing down towards the substrate (P_{down}). The outermost part of diagram without an applied tip voltage represents the spontaneous polarization state of as-grown PZT thin films. Therefore, the polarization of self-poled PZT gradually switches from P_{down} to P_{up} with increasing film thickness from 8 nm to 130 nm. For the 48 nm PZT, a mixed polarization (P_{mix}) of P_{down} and P_{up} indicates the transition point of the switching of polarization. The details of the change of polarization direction as a function of PZT thickness and the experimental setup are shown in Figures S5a-S5f of SM.

Since PFM results provide the ferroelectric properties in a large thin film volume, STEM was employed to study the local information of self-poled PZT films. As shown in Figures 3d-3f, STEM-ABF images were viewed along the [010] direction from the PZT films with three different thicknesses, showing the projection of Ti/Zr (red open circles) and oxygen (blue open circles) atoms. The detailed information may be found in Figures S6a-S6f of SM. At the portion of film near the LSMO/PZT interface, the polarization direction around the interface is evident. It is found that P_{down} and P_{up} coexist in both 48 nm and 130 nm PZT, while the uniform P_{down} state is presented in 8 nm PZT. These observations are consistent with the out-of-plane PFM results, especially in the 8 nm and 48 nm PZT films. We note that the probing depth of the PFM measurement dramatically depends on dielectric permittivity of FE materials and contact conditions between the tip and the sample surface [39, 40]. According to Kalinin et al [41], the tip-induced electroelastic field drops within a distance of approximately 100 nm for $PbZr_{1-x}Ti_xO_3$, resulting in a finite probing depth. Hence, for 130 nm film, the PFM shows the upward polarization in the large thin film volume of PZT, which is not

in conflict with the coexistence of P_{down} and P_{up} around the LSMO/PZT interface revealed by STEM-ABF imaging.

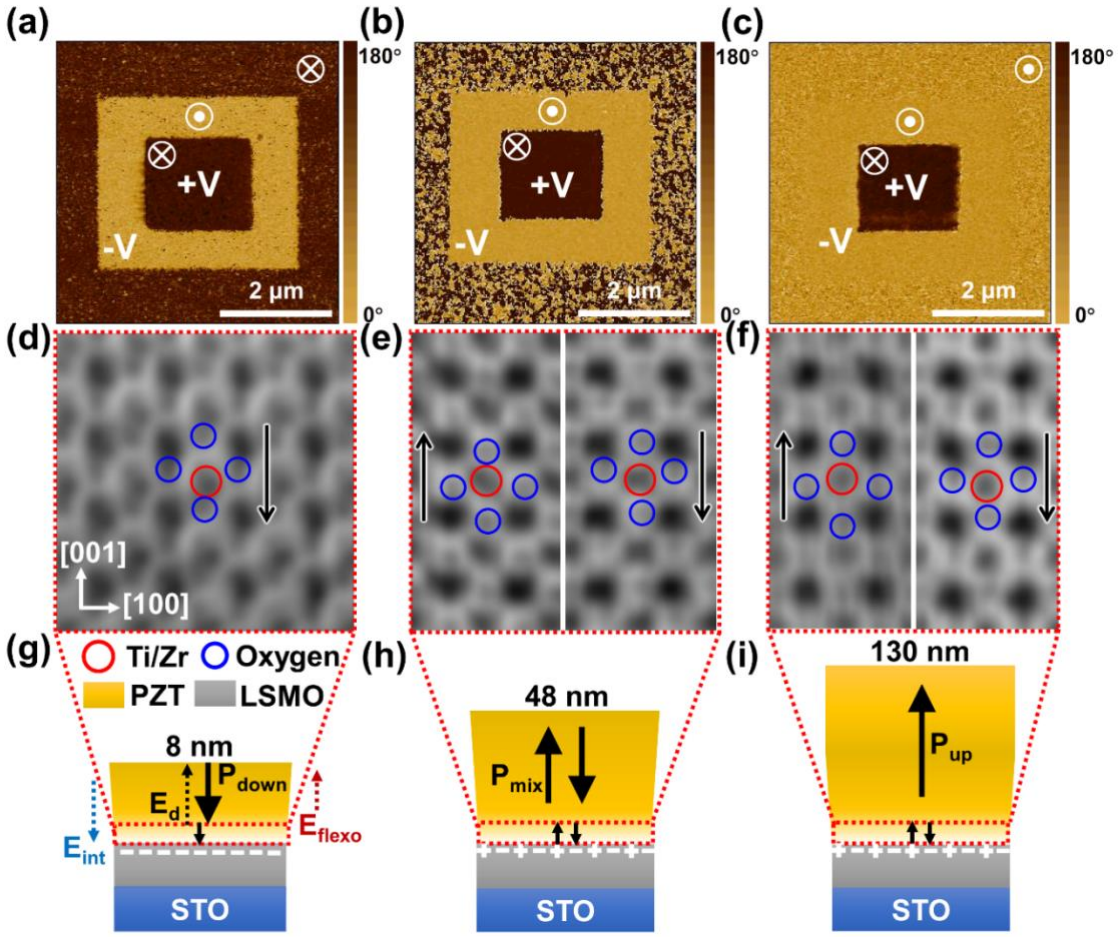

Figure 3. Room temperature out-of-plane PFM diagrams and STEM-ABF images viewed along the [010] direction near the LSMO/PZT interface for samples with three different thicknesses of PZT: (a,d) 8 nm (b,e) 48 nm (c,f) 130 nm. P_{down} is denoted by ⊗ and P_{up} is denoted by ⊙. Panel (d)-(f) are the magnified portions of the STEM-ABF images of the PZT film near the LSMO/PZT interface (see the details in Figure S6). The arrows indicate the polarization direction near the LSMO/PZT interface, where LSMO is below the PZT layer. The red open circles correspond to Ti/Zr atoms and the blue open circles represent oxygen atoms. (g)-(i) Schematic illustrations of three sample configurations, showing the polarization-induced charge screening in the interfacial LSMO. The plus sign indicates the hole and the minus sign corresponds to the electron. The large black arrows indicate the polarization direction of large thin film volume of PZT, while the small black arrows correspond to polarization direction near the LSMO/PZT interface marked by the red-dotted rectangle. E_d is the depolarization field, E_{int} is the built-in electric field, and E_{flexo} is the flexoelectric field.

Both PFM and STEM results show that the direction of polarization changes with the PZT film thickness, as summarized in Figures 3g-3i. Several

mechanisms, including the interfacial electric field induced by the bottom electrode, the evolution of the strain effects, the interface termination, and charged defects such as oxygen vacancies in FE films [38, 42-44], have been proposed for the self-poling phenomenon. It is well known that PZT thin film may suffer from the non-stoichiometric concentrations due to lead or oxygen vacancies during the deposition process [45, 46] and may be considered as a wide band-gap semiconductor [47]. The depletion region may form when the PZT contacts with the hole-doped metallic LSMO [48], which is analogous to the case of p-n/Schottky junction [49]. A simplified band alignment for the LSMO/PZT interface is illustrated in Figure S7 of SM, based on previous studies [50-52]. The depletion region would bend the band structure, forming the built-in electric field (E_{int}) directed from the PZT to the bottom electrode LSMO. Consequently, the E_{int} may polarize the PZT into the P_{down} state. Due to the low concentration of charge carriers in PZT and the high density of holes in LSMO film, the depletion region is mainly located in PZT and its width ranging from 3-35 nm depending on the charge carriers densities, the Ti/Zr ratio, and the ground state of the bottom electrode [47, 49]. This built-in electric field plays a dominant role in the self-poling of thin PZT films (< 48 nm), and there is an opposite depolarization field (E_d) accompanied with the polarization, as shown in Figure 3g. When the thickness of PZT increases, the interfacial effect gradually diminishes while the evolution of strain status needs to be considered. The strain gradient points in the direction from the substrate to the film surface, thus generating a corresponding E_{flexo} in the direction of the strain gradient, which favors the upward polarization [13].

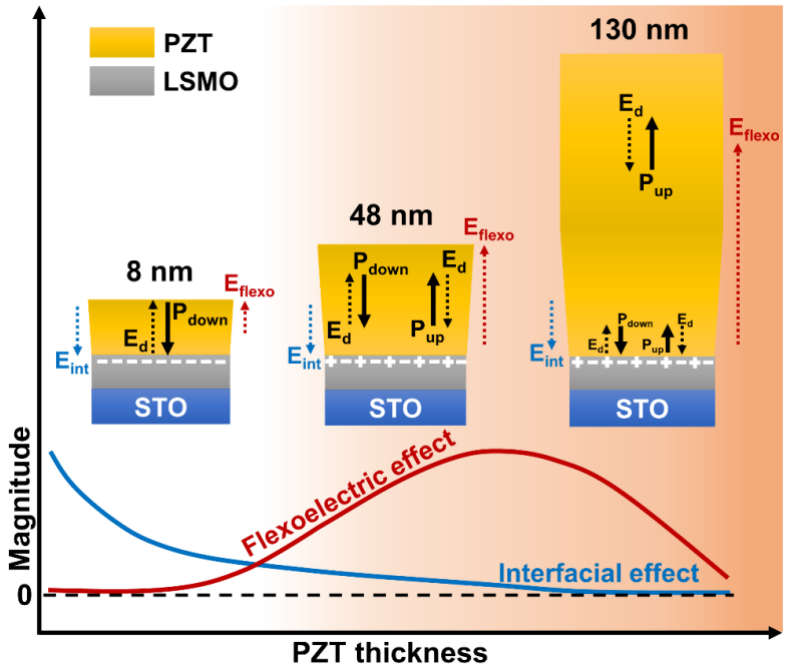

Figure 4: Schematic illustrations of three samples configurations and the competition between E_{int} (blue curve) and E_{flexo} (red curve) as a function of PZT thickness. E_d is the depolarization field, E_{int} is the built-in electric field, and E_{flexo} is the flexoelectric field. The solid arrows indicate the polarization direction and the dotted arrows correspond to the electric fields. The magnitude of the polarization and the electric fields are independent of the arrow size.

In the current study, this flexoelectric effect works in tandem with the E_d against the interfacial effect, attempting to switch the polarization from the downward direction to the upward direction, as illustrated in Figure 4. The changing magnitude of E_{flexo} was roughly estimated based on the Figure 2i. In the thinner PZT films, the large E_{int} competes with a small E_{flexo} and induces a downward polarization P_{down} in 8 nm PZT. With an increase of thickness, the strain relaxation occurs thus E_{flexo} starts to increase and reaches the highest value at a critical thickness. The large E_{flexo} overrides the interfacial effect and turns the polarization orientation from pointing downwards to upwards. Therefore, a mixture of P_{up} and P_{down} is present in the 48 nm PZT and the region near the LSMO/PZT interface in the case of 130 nm PZT sample. With further increase of thickness, the E_{flexo} begins to drop due to the totally relaxed strain status in the thicker films and the polarization direction maintains upward, as shown in the large thin film volume of 130 nm PZT far away from the LSMO/PZT interface.

Other possible effects, such as the depolarization field effect [42], the charge on the PZT/air surface [52], and the non-switchable layer of PZT [53] may need to be considered together with the effects of E_{int} and E_{flexo}. These cooperative effects warrant further investigation and that is beyond the current scope of our paper. To sum up, the thickness could effectively tune the polarization direction of PZT films, and its effect on ME coupling in the LSMO/PZT heterostructures is discussed as follows.

D. Interfacial charge-mediated effects

Combing the above results, the T_c and M_s of LSMO are largely enhanced with 8 nm PZT in the P_{down} state, whereas they are weakened most with 130 nm PZT in the mixed polarization state at the LSMO/PZT interface. In addition, the enhanced resistivity is clearly observed in the mixed state, as compared to that in the P_{down} state. It has been demonstrated that out-of-plane FE polarization is screened in the manganite within a few unit cells from the interface, leading to two possible interfacial states: depletion or accumulation of charge carriers [54]. Therefore, PZT thickness-dependent polarization may electrostatically modulate the hole carrier density of interfacial LSMO, resulting in the depletion of holes with 8 nm PZT and the mixture of electrons and holes with 48 nm and 130 nm PZT, as illustrated in Figures 3g-3i.

In order to examine the interfacial-charge screening effect, room temperature XANES measurement on the entire thin film layer, collected in the TFY mode, was employed. Figure 5a shows the typical Mn *K*-edge XANES spectrum of LSMO with different thicknesses of PZT films, consisting of a pre-edge peak (~ 6540 eV) and a sharp rising edge with a maximum resonance peak E_r (~ 6555 eV). It is known that Mn *K*-edge main absorption edge arises from the transition from 1*s* core level to unoccupied 4*p* orbitals. The main edge position is found to vary with the doping level *x* of mixed-valence manganites [55, 56]. In

general, it shifts to the higher energy position when Mn^{4+} content increases. Compared with pure LSMO sample (0 nm PZT), a measurable shift of the inflection point to a lower energy position (~ 0.2 eV) is observed in LSMO with 8 nm PZT. Correlatively, an appreciable E_r shifting to a lower energy (~ 0.3 eV) is recognized in LMSO with 8 nm PZT, together with an increased amplitude of this resonance peak. These observations indicate a decrease in the averaged valence state of Mn with 8 nm PZT, as compared to that of pure LSMO. It is in line with above results that 8 nm PZT in the P_{down} state may induce the depletion of holes in the interfacial region of LSMO (Figure 3g). Based on the reported linear relationship [57] between the edge shift and the doping level *x*, $\Delta E = 3.0x$, an increase of 0.08 ± 0.03/Mn in the averaged valence state is estimated for the LSMO in holes depletion state, and hence an averaged increase of 0.08 ± 0.03 μ_B/Mn is induced by valence modulation, as compared to the pure LSMO sample. Although the interfacial holes depletion indeed enhances magnetism as supported by SQUID results, this calculated change of Mn moments from the charge screening effect is smaller than that measured by SQUID (i.e. an increase of 0.46 ± 0.12 μ_B/Mn), as shown in Figures 1b-1c. Furthermore, the decrease of magnetization for LSMO with 130 nm PZT is not consistent with the overall change of chemical valence.

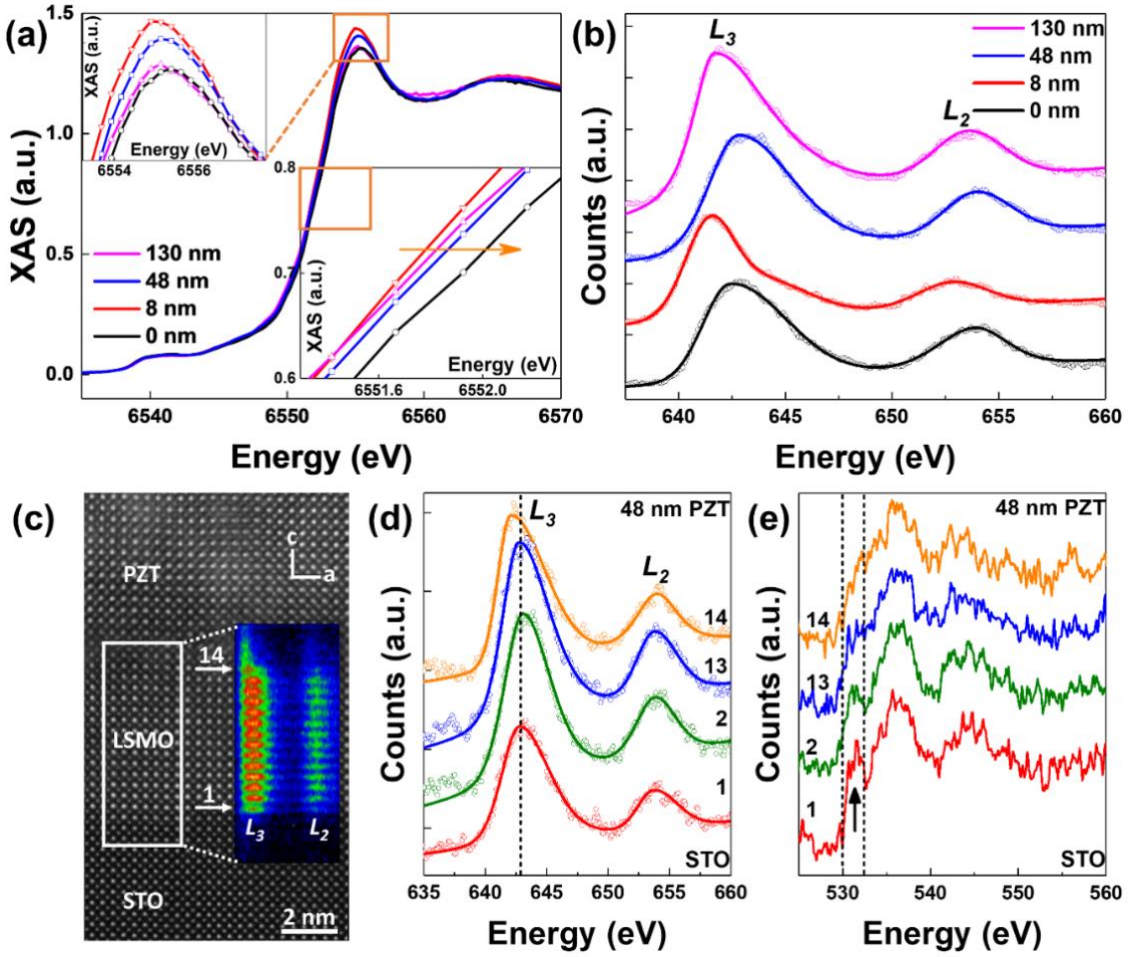

Figure 5. (a) The Mn *K*-edge XANES spectra of LSMO with 0 nm, 8 nm, 48 nm and 130 nm PZT, respectively. The insets show the enlarged part of the maximum peak and the position of inflection point. (b) EELS of Mn $L_{3,2}$-edge of LSMO with 0 nm, 8 nm, 48 nm and 130 nm PZT, respectively. (c) The STEM-HAADF image of STO/LSMO/PZT (48 nm) sample. The inset is the EELS spectral image of Mn $L_{3,2}$-edge averaged vertically from the area marked by the rectangle. The numbers indicate the position of atomic Mn columns starting from the STO/LSMO interface. The number 1 corresponds to the first Mn column of LSMO at the STO/LSMO interface and number 14 corresponds to the last Mn column of LSMO at the LSMO/PZT interface. (d) Mn $L_{3,2}$-edge and (e) O *K*-edge EELS spectra of LSMO with 48 nm PZT, respectively, collected at selected Mn columns of LSMO near the STO/LSMO (number 1 and 2) and the LSMO/PZT interface (number 13 and 14). The pre-peak feature is denoted by the arrow.

The averaged XANES is insufficient to explain the experimental results, then the detailed information about local valence changes was obtained from the Mn $L_{3,2}$-edge EELS. The chemical shift of Mn $L_{3,2}$-edge arises from the changes in the core-level energy and the effective charges on the atom [58]. As shown in Figure 5b, Mn $L_{3,2}$-edge spectra (circles) were achieved by averaging the whole

LSMO layer. The solid lines are the refinement by asymmetric Gaussian and Lorentzian function with refined L_3 peaks at 642.42 eV, 641.41 eV, 642.78 eV and 641.66 eV (from bottom to top) with an increase of PZT thickness, respectively. Standard error of each fitting was used to calculate the error bars (± 0.06 eV). Generally, the lower the L_3 energy position, the lower the averaged valence state of Mn [14, 20]. Therefore, LSMO with 8 nm PZT has the lowest valence state of Mn, which is well-matched with Mn *K*-edge XANES results. Compared with the LSMO with 8 nm PZT, a noticeable positive shift for the 48 nm PZT sample (~ 1.37 eV) and a less significant one (~ 0.25 eV) for the 130 nm PZT sample are observed.

Besides the averaged EELS, the change of interfacial valence was also investigated. Figure 5c shows the STEM-HAADF image of STO/LSMO (14 u.c.)/PZT (48 nm) sample and the atomic scale EELS mapping of Mn $L_{3,2}$-edge in the selected zone. The sharp interface may be observed with little Mn intermixing. These index numbers indicate the position of atomic columns, where the Mn $L_{3,2}$-edge and the O *K*-edge fine structures were collected from. As shown in Figure 5d, in the case of LSMO with 48 nm PZT, the L_3 peak positions are 642.76 eV, 643.03 eV, 642.72 eV and 642.05 eV from the bulk LSMO (number 1, 2) to the Mn columns near the LSMO/PZT interface (number 13, 14). The error bars are ± 0.1 eV. The L_3 edge shifts to the lower energy position (~ 0.7 eV) from the bulk LSMO to the LSMO/PZT interface, indicating a lower valence state of interfacial LSMO than that of the bulk layer. This agrees with the proposed built-in electric field accompanied with the negative charge aggregation at LSMO side of the LSMO/PZT interface. Similar observations for the LSMO with 8 nm and 130 nm PZT are shown in Figures S8a-S8b of SM.

In addition, O *K*-edge fine structures collected from the number 1,2 and number 13, 14 are shown in Figure 5e. Pre-peak feature of the O *K*-edge, which is correlated with the hybridization of O 2*p* with Mn 3*d* bands, is sensitive to the

valence of the Mn [59]. A linear relationship between the pre-peak intensity and the valence of Mn in manganites has been reported [60], where the pre-peak intensity increases when the valence of Mn increases. Figure 5e shows that the pre-peak of LSMO with 48 nm PZT gradually diminishes from the bulk LSMO (number 1,2) to the LSMO/PZT interface (number 13, 14), indicating a lower valence of interfacial Mn than that of the bulk thin film layer. The suppression of pre-peak feature near the LSMO/PZT interface is also noticed for the LSMO with 8 nm and 130 nm PZT, as shown in Figures S8c-S8d. In particular, the pre-peak feature is almost missing for the entire LSMO thin film layer with 8 nm PZT (Figure S8c). In comparison, the visible pre-peak feature in the case of 48 nm PZT sample near the LSMO/PZT interface (number 13 of Figure 5e) suggests a higher valence state of Mn than that of 8 nm PZT sample.

From both XANES and EELS results, the averaged valence of Mn is found to vary with PZT thickness-dependent polarization. The layer-resolved EELS results suggest the non-uniformity of electronic structures in the LSMO films due to the interfacial coupling. Nevertheless, the increased magnetic moments may not be quantitatively explained by the interfacial charge-mediated effects. Considering the strong correlation between the electronic structure and crystal structure, additional mechanisms, such as the strain-mediated structural deformation including MnO_6 octahedral rotation and orbital reconstruction across the LSMO/PZT interface, may be responsible for the change of magnetic properties in our study.

E. Local structural deformation in LSMO

Due to the intrinsic strong coupling between the strain and polarization in FE materials, the strain-mediated effects may apply to LSMO through the lattice mismatch, octahedral connectivity, atomic displacement, and orbital hybridization across the LSMO/PZT interface [12, 14, 15]. According to the XRD results, all LSMO thin films are fully strained by the STO substrate. Considering

the fixed thickness of LSMO, the strain effect from the STO substrate is assumed to be constant for all the samples. In this study, we focus on the strain-mediated effects induced by the overlying PZT thin films.

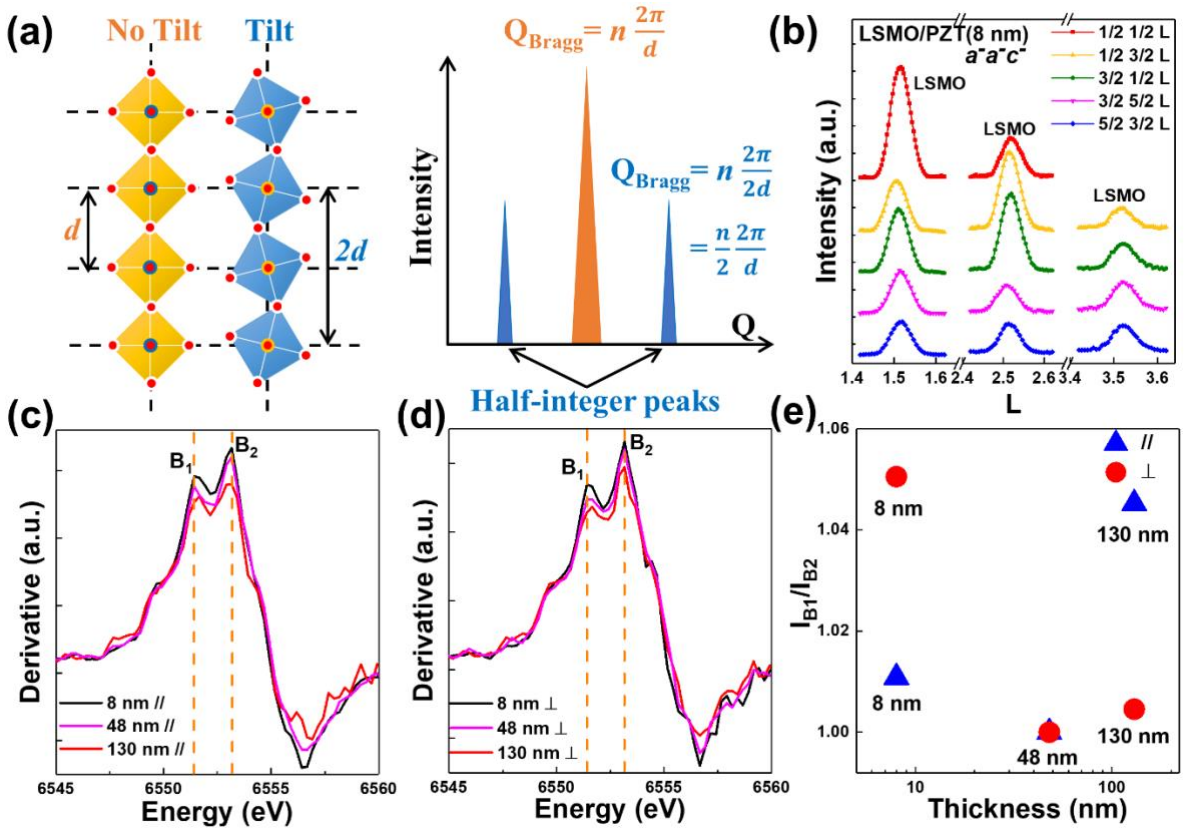

Figure 6. (a) Schematic illustration of the MnO_6 octahedral tilt and the appearance of half-integer peaks. Q is the transfer momentum in Bragg's law, *d* is the periodic length, and *n* is an integer number determined by the order of diffraction. (b) Room temperature half-integer diffraction measurement of STO/LSMO/PZT (8 nm) heterostructure. X-ray energy is 20 keV. The derivative curves of polarized Mn *K*-edge XANES spectra of LSMO with 8 nm, 48 nm and 130 nm PZT in (c) parallel (//) and (d) perpendicular (⊥) measurement. In parallel measurement, ***E*** vector of incident x-ray is along the film plane; in perpendicular case, ***E*** vector is perpendicular to the film plane. (e) Summary of the intensity ratio of B_1/B_2 in the two polarization directions of Mn *K*-edge XANES spectra, normalized by the value of LSMO with 48 nm PZT for a comparison.

The depth profile of the out-of-plane lattice spacings of LSMO, which vary across the LSMO/PZT interface, strongly depends on the thickness of overlying PZT films (see the details in Figure S9 of SM). The averaged out-of-plane lattice constants of LSMO are slightly changed (~0.5%) with increasing PZT thickness (Figure S4). Half-integer diffraction measurement, developed by Glazer in the

1970s [61, 62], was employed to characterize the MnO_6 octahedral rotation with increasing PZT thickness. As illustrated in Figure 6a, the presence of octahedral tilt results in the doubling of periodicity (2*d*) along certain axes [61, 63]. Half-integer peaks due to the oxygen scattering may be separated from the strong intensity of the cations scattering, since the periodic length of the cations remains constant (*d*). Figure 6b shows a series of clear half-integer peaks in the STO/LSMO/PZT (8 nm) heterostructure. The half-integer diffractions of more samples are shown in Figures S10a-S10c of SM. By examining the presence/absence of the specific half-integer peaks, the octahedral rotation patterns of LSMO were identified as $a^-a^-c^-$ in all the samples according to the Glazer notation [27, 62].

Based on the previous studies [64-66], experimental half-integer peak intensities were used to calculate the tilt angles and oxygen positions by the home-made codes [67] (see the details in Table SI and Figures S11a-S11c in SM). Calculated tilt angles, bond lengths and bond angles of MnO_6 with the error bars are summarized in the Table II. With an increase of PZT thickness, both the in-plane and out-of-plane tilt angles of MnO_6 gradually decrease. Thicker PZT film seems to exert a damping effect on MnO_6 rotation, which induces the smallest out-of-plane bond length in the LSMO with 130 nm PZT. Consistently, the ratio of the out-of-plane bond length to the in-plane bond length (d_{out}/d_{in}) is found to be smaller in the LSMO with 130 nm PZT than that of LSMO with 8 nm and 48 nm PZT. In comparison, LSMO with 8 nm PZT has the largest out-of-plane bond length and d_{out}/d_{in} ratio. The half-integer results reveal that anisotropic bond length of MnO_6 is induced by the PZT thickness-dependent strain-mediated effects, which may further affect the electron hopping and magnetic properties of LSMO.

Table II. Summary of bond length ($d_{Mn\text{-}O}$), bond angle (α_B, γ_B), and octahedral rotation angle (α_T, γ_T) of the LSMO with 8 nm, 48 nm and 130 nm PZT, along the in-plane and out-of-plane direction. d_{out}/d_{in} is the ratio of the out-of-plane $d_{Mn\text{-}O}$ to the in-plane $d_{Mn\text{-}O}$ value. The experimentally measured Curie temperature T_c and the calculated electron hopping probability $t_{d\text{-}d}$ between neighboring Mn sites of LSMO with 8 nm, 48 nm and 130 nm PZT are normalized by the value of LSMO with 48 nm PZT.

Sample	In-plane			Out-of-plane			$\frac{d_{out}}{d_{in}}$	$\frac{T_c}{T_{c,48\ nm}}$	$\frac{t_{d-d}}{t_{d-d,48\ nm}}$
	d_{Mn-O} (Å)	α_B (°)	α_T (°)	d_{Mn-O} (Å)	γ_B (°)	γ_T (°)		Exp.	Cal.
LSMO 8nm PZT	1.972 (± 0.012)	164.0 (± 2.8)	5.8 (± 0.4)	1.921 (± 0.011)	163.9 (± 3.7)	5.7 (± 0.9)	0.974 (± 0.001)	1.05 (± 0.01)	1.03 (± 0.05)
LSMO 48nm PZT	1.969 (± 0.012)	165.1 (± 2.3)	5.7 (± 0.7)	1.919 (± 0.012)	163.8 (± 3.4)	5.0 (± 1.3)	0.974 (± 0.001)	1	1
LSMO 130nm PZT	1.967 (± 0.009)	166.2 (± 3.2)	5.0 (± 0.4)	1.906 (± 0.008)	165.9 (± 3.2)	4.8 (± 0.5)	0.969 (± 0.001)	0.95 (± 0.01)	0.97 (± 0.04)

F. Strain-modulated electronic structure in LSMO

Polarization-dependent Mn *K*-edge XANES was then utilized to probe the strain-mediated effects on the electronic structure of LSMO, due to the fact that the detailed shape of curves is associated with the strong hybridization of Mn 3*d* orbitals and O 2*p* orbitals [68-70]. Figures 6c-6d show that, in the two polarization directions, two sub-peaks (as denoted by B_1 and B_2) are observed in the derivative curves of Mn *K*-edge XANES of all three samples. The lower energy peak B_1 corresponds to the $3d^{n+1}\underline{L}4p^1$ electron configuration due to the Coulomb interaction between the Mn 1*s* core hole (due to the x-ray photon excitations) and extra 3*d* electron, whereas the higher energy peak B_2 corresponds to $3d^nL4p^1$ electronic state [65, 71]. Here, *L* indicates the oxygen ligands, and $\underline{L}$ means one hole in the oxygen ligands resulting from electron transfer from O 2*p* orbitals to Mn 3*d* orbitals. It is known that intensity ratio of B_1/B_2 is correlated with the strain-induced anisotropy of local structure environment, which may further make the hybridization between O 2*p* and Mn 3*d* orbitals anisotropic inside the MnO_6 octahedra. In general, the higher intensity ratio of B_1/B_2, the

larger Mn-O charge transfer probability. As summarized in Figure 6e, LSMO with 8 nm PZT has a higher B_1/B_2 value in the perpendicular measurement; in the parallel case, LSMO with 130 nm PZT has a higher B_1/B_2 value. LSMO with 48 nm PZT is taken as a reference with the lowest B_1/B_2 ratio in the both polarization directions. Based on our previous work [65, 70], the dominant Mn-O charge transfer channel is the in-plane process (from O $2p_x$, $2p_y$ orbitals to Mn $3d_{x^2-y^2}$ orbitals) for the perpendicular measurement and that is the out-of-plane process (from O $2p_z$ orbitals to Mn $3d_{3z^2-r^2}$ orbitals) for the parallel measurement. Therefore, LSMO with 8 nm PZT has a higher in-plane Mn-O hopping integral whereas the LSMO with 130 nm PZT has a higher out-of-plane Mn-O hopping probability. The enhancement of charge transfer is in the direction where a larger overlap between O 2*p* and Mn 3*d* orbitals (i.e. a smaller Mn-O bond length). It is supported by the half-integer results that d_{out}/d_{in} is smaller in the LSMO with 130 nm PZT than that of LSMO with 8 nm PZT.

The anisotropic Mn-O charge transfer is closely associated with preferential electron occupancy of Mn 3*d* orbital, which could be taken into account for T_c calculation [72]. According to the study of Chen et al [73], a larger Mn-O hopping probability results in a higher center-of-band energy and a less occupancy considering the fact that in LSMO two Mn e_g states are antibonding in nature. In this context, LSMO with 8 nm PZT, with a larger d_{out}/d_{in} and a higher in-plane Mn-O hopping, relatively prefers the out-of-plane orbital occupancy; LSMO with 130 nm PZT, with a smaller d_{out}/d_{in} and a higher out-of-plane Mn-O hopping, relatively prefers the in-plane orbital states. The polarized XANES results provide evidences of the strain-mediated effects on the Mn-O charge transfer and preferential electron occupancy of Mn 3*d* orbitals, which are not easy to be detected by x-ray linear dichroism due to the thick PZT overlayers.

G. Discussion on magnetism

It is well known that in the framework of double-exchange interaction, T_c in the metallic manganites is proportional to the electron hopping probability between two nearest Mn sites ($t_{d\text{-}d}$), which is determined by the orbital overlap between the Mn *3d* and O *2p* orbitals. The PZT thickness-dependent strain-mediated effects on the Mn-O bond length, Mn-O-Mn bond angle, and Mn 3*d* orbital occupancy may modulate the electron hopping and therefore T_c of LSMO, according to the following equation [65, 72]:

$$
\begin{aligned}
T_c \propto t_{d-d} &= \sum_{i,j} \chi(\varphi_i)\chi(\varphi_j^{'})V_{pd}^2 \\
&= \frac{1}{6}\{4\cdot\sin^2(\frac{\alpha_B}{2})\cdot d_{Mn-O,in}^{-7}\cdot n_{x^2-y^2}\cdot\chi(x^2-y^2)\cdot[\chi(x^2-y^2)+\chi(3z^2-r^2)] \\
&\quad +4\cdot\sin^2(\frac{\alpha_B}{2})\cdot d_{Mn-O,in}^{-7}\cdot(1-n_{x^2-y^2})\cdot\chi(3z^2-r^2)\cdot[\chi(x^2-y^2)+\chi(3z^2-r^2)] \\
&\quad +2\cdot\sin^2(\frac{\gamma_B}{2})\cdot d_{Mn-O,out}^{-7}\cdot(1-n_{x^2-y^2})\cdot\chi(3z^2-r^2)\cdot\chi(3z^2-r^2)\}
\end{aligned}
\qquad (1)
$$

where $\chi(\varphi_i)$ is the probability of e_g electron transferring from the φ_i orbital of *i* Mn ion ($\varphi = 3d_{3z^2-r^2}$ or $3d_{x^2-y^2}$) to an O 2*p* orbital, and $\chi(\varphi_j')$ is the probability of e_g electron hopping from an O 2*p* orbital to the φ_j' orbital in the neighboring *j* Mn ion. V_{pd} is the matrix element between *p* and *d* orbitals and it is proportional to $d_{Mn-O}^{-3.5}$. $n_{x^2-y^2}$ is the ratio of electron occupancy in Mn $3d_{x^2-y^2}$ orbital. The transfer intensity $\chi(\varphi_i)$ and $\chi(\varphi_j')$ may refer to previous studies [72]. It is worth noting that $t_{d\text{-}d}$ is determined by not only the Mn-O bond length and Mn-O-Mn bond angle along both the in-plane and the out-of-plane directions, but also the electron occupancy in Mn 3*d* orbitals as well. Based on the above discussion that LSMO with 8 nm PZT relatively prefers the out-of-plane orbital occupancy while LSMO with 130 nm PZT relatively prefers the in-plane orbital states, the assumptions of $n_{x^2-y^2}$ = 0 for the LSMO with 8 nm PZT, 0.5 for the LSMO with 48 nm PZT, and 1 for the LSMO with 130 nm PZT, are used. As shown in Table II, the changing trend of calculated $t_{d\text{-}d}$ is well-matched with the experimentally

measured T_c, where the LSMO with 130 nm PZT has the smallest $t_{d\text{-}d}$ and the LSMO with 8 nm PZT has the highest value. The small difference may result from the rough assumption of ratio of electron occupancy in Mn 3*d* orbitals. This calculation demonstrates that strain-mediated effects on the bond length/angle of MnO_6 and the Mn 3*d* orbital occupancy work in synergic to modulate T_c of LSMO thin films.

As it is well known, the magnetic configuration depends on a delicate balance between the ferromagnetic and the antiferromagnetic (AFM) spin coupling. Additional effects, such as spin exchange coupling, modified by the variation of charge carrier density [74, 75] or the interfacial orbital reconstruction [11, 15], could appear with the change of Curie temperature. The spin ordering in the strained manganites is affected by the orbital preferential occupancy. According to the above results, the preferential Mn $3d_{x^2-y^2}$ ordering in the LSMO with 130 nm PZT may stabilize A-type antiferromagnetic spin configuration, where spins couple ferromagnetically in the plane and antiferromagnetically along the out-of-plane direction [76]. It may lead to the depression of double-exchange mechanism and magnetization of LSMO [77]. In order to investigate the spin exchange coupling, the measurements of zero field cooling and field cooling magnetic hysteresis loops were conducted.

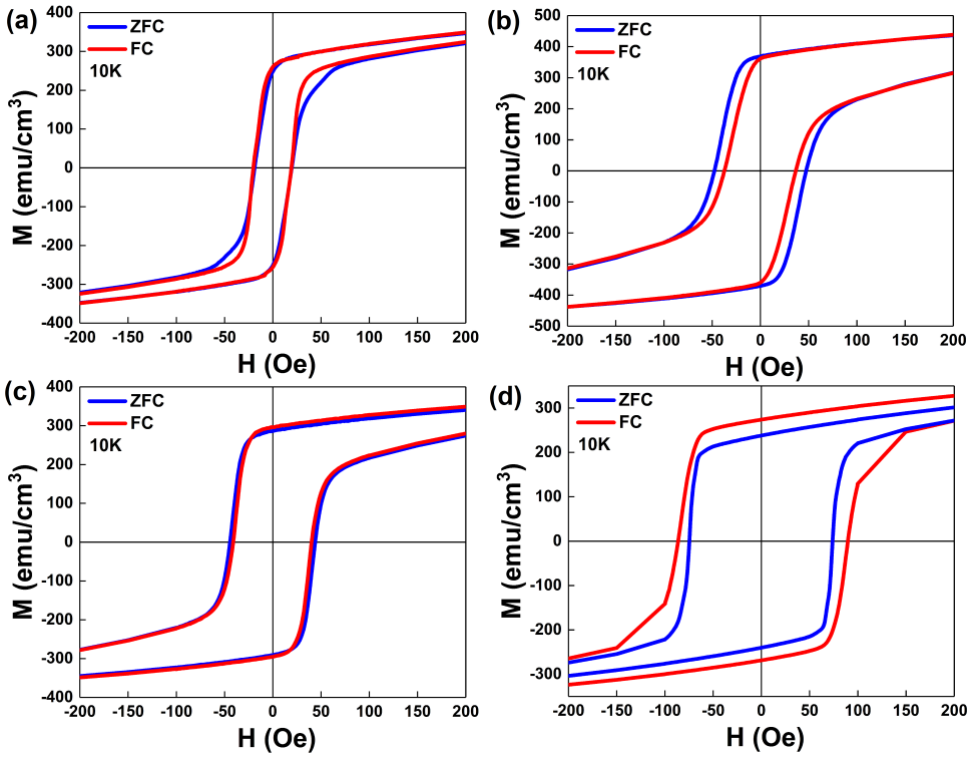

Figure 7: Measurements of zero field cooling (ZFC) and field cooling (FC) magnetization loops of (a) pure LSMO (b) LSMO/PZT (8 nm) (c) LSMO/PZT (48 nm) and (d) LSMO/PZT (130 nm) were conducted at T=10 K. The field cooling was applied with 5 T magnetic field. The measurement step size is 1 Oe.

Figures 7a-7c show no exchange bias in the pure LSMO, LSMO with 8 nm and 48 nm PZT films, respectively. In comparison, a small exchange bias (~1.7 Oe, $H_E = |H_{C1}+H_{C2}|/2$ where H_{C1} and H_{C2} are the forward and reversed coercive fields of magnetization hysteresis loops) with an obvious enhancement of coercivity, as a typical phenomenon associated with the exchange anisotropy induced at the FM/AFM interface [78], is observed in the LSMO with 130 nm PZT (Figure 7d). Considering the measurement step size is 1 Oe, this small value of exchange bias is trustworthy. In LSMO thin films (~14 u.c.), the thickness of antiferromagnetic (AFM) layers may be very small, leading to the weak AFM anisotropy [78]. The ferromagnetic layer would drag small AFM spins when it rotates during the magnetic hysteresis loop, resulting in an obvious increase in the coercivity with a small loop shift. The presence of positive exchange bias (shift of the magnetic hysteresis loop in the same direction as the applied +5 T

magnetic fields) may result from the antiferromagnetic coupling at the interface between the FM and AFM layers [78, 79]. Unlike the large exchange bias found in the LSMO with antiferromagnetic $BiFeO_3$ films [80], the presence of antiferromagnetic spin coupling may arise from the LSMO/PZT interface through the orbital reconstruction. Therefore, the strain-mediated effects on the bond length/angle of MnO_6 accompanied with a modified spin exchange coupling enables the PZT thickness-dependent modulation of magnetic properties of LSMO. Apart from T_c, the decreased magnetization in the LSMO with 130 nm PZT may be explained by the strain effects on the spin configuration of the Mn atoms.

Combining the above charge-mediated and strain-mediated effects, the polarization-driven carrier density modulation at the LSMO/PZT interface and the strain-mediated Mn 3*d* orbital occupancy work together to enhance magnetism of LSMO with PZT thickness < 48 nm. The strain-induced modulations in the bond length/angle of MnO_6 accompanied with a modified spin configuration are responsible for the decrease in the Curie temperature and magnetization of LSMO with PZT thickness > 48 nm. It is noted that PZT thickness-dependent strain-mediated effects on LSMO are realized through the polarization-associated local structure distortions, which are resulted from the lattice mismatch, octahedral rotation, atomic displacement, orbital hybridization, and polarization-induced charge screening effect. In the current study, for LSMO with PZT < 48 nm, the local distortion is mainly correlated with the charge carrier redistribution and orbital reconstruction driven by polarization. For LSMO with PZT > 48 nm, the evolution of strain status in the thick PZT film couples to the underlying LSMO through the modulations of lattice constants and MnO_6 octahedral rotation with the modified bond lengths/angles across the interface. To differentiate the entangled effects of polarization and strain at the interface, further work of different ferroelectric materials with the controlled polarization

direction is warranted, which is beyond the scope of the current work. In our study, the reversal of polarization is realized by changing PZT thickness, without the cumbersome design of devices required for application of an electric field. Hence, it is an attractive alternative approach to observe intrinsic ME coupling in FM/FE heterostructures.

IV. SUMMARY

The thickness-dependent polarization of PZT films results in noticeable effects on intrinsic magnetoelectric coupling in the LSMO/PZT heterostructures. The competition between the interfacial built-in field and the flexoelectric field is proposed to explain the polarization switching. With thin PZT films < 48 nm, the polarization-driven valence modulation and strain-mediated Mn 3*d* orbital occupancy work together to enhance magnetism of LSMO thin films; with thick PZT films > 48 nm, the strain-induced modifications of bond length/angle of MnO_6 associated with a modified spin configuration are responsible for the suppressed Curie temperature and magnetization of LSMO. The study of competition/cooperation of charge and strain-mediated effects in the LSMO/PZT heterostructures sheds light on the entangled interplay between the charge, lattice, orbital, and spin in strongly correlated oxides. Our work provides a viable means to induce desirable magnetoelectric effects in FM/FE heterostructures, with promising potentials in applications such as spintronic memory and logic devices.

ACKNOWLEDGMENTS

The research was supported by the Singapore Ministry of Education Academic Research Fund Tier 2 under the project No. MOE2015-T2-1-016 and the project No. MOE2018-T2-1-019, MoE T1 R-284-000-196-114, and the Singapore National Research Foundation under CRP Award No. NRF-CRP10-2012-02. The support of Singapore Synchrotron Light Source (SSLS), a National Research Infrastructure under the National Research Foundation Singapore, is acknowledged. Work at Brookhaven National Laboratory was supported by the U.S. Department of Energy, Office of Basic Energy Science, Division of Materials Science and Engineering, under Contact No. DESC0012704. Use of the Advanced Photon Source, an office of Science User Facility operated for the U.S. Department of Energy (DOE) Office of Science by Argonne National Laboratory, was supported by the U.S. DOE under Contact No. DE-AC02-06CH11357. We thank Dr. John W. Freeland for his kind support at beamline 4-ID-C of Advanced Photon Source.

Xiaoqian Yu, Lijun Wu, and Bangmin Zhang contributed equally to this work.

References:

[1] S. A. Wolf, D. D. Awschalom, R. A. Buhrman, J. M. Daughton, S. von Molnar, M. L. Roukes, A. Y. Chtchelkanova and D. M. Treger, Science **294**, 1488 (2001).
[2] R. Ramesh and N. A. Spaldin, Nat. Mater. **6**, 21 (2007).
[3] G. A. Prinz, Science **282**, 1660 (1998).
[4] V. Garcia, M. Bibes, L. Bocher, S. Valencia, F. Kronast, A. Crassous, X. Moya, S. Enouz-Vedrenne, A. Gloter, D. Imhoff, C. Deranlot, N. D. Mathur, S. Fusil, K. Bouzehouane and A. Barthelemy, Science **327**, 1106 (2010).
[5] W. Eerenstein, M. Wiora, J. L. Prieto, J. F. Scott and N. D. Mathur, Nat. Mater. **6**, 348 (2007).
[6] J. Ma, J. Hu, Z. Li and C. W. Nan, Adv. Mater. **23**, 1062 (2011).
[7] C. A. Vaz, J. Phys. Condens. Matter **24**, 333201 (2012).
[8] H. J. A. Molegraaf, J. Hoffman, C. A. F. Vaz, S. Gariglio, D. van der Marel, C. H. Ahn and J.-M. Triscone, Adv. Mater. **21**, 3470 (2009).
[9] C. A. Vaz, J. Hoffman, Y. Segal, J. W. Reiner, R. D. Grober, Z. Zhang, C. H. Ahn and F. J. Walker, Phys. Rev. Lett. **104**, 127202 (2010).
[10] B. Cui, C. Song, H. Mao, Y. Yan, F. Li, S. Gao, J. Peng, F. Zeng and F. Pan, Adv. Funct. Mater. **26**, 753 (2016).
[11] D. Preziosi, M. Alexe, D. Hesse and M. Salluzzo, Phys. Rev. Lett. **115**, 157401 (2015).
[12] B. Zhang, L. Wu, W. G. Yin, C. J. Sun, P. Yang, T. Venkatesan, J. Chen, Y. Zhu and G. M. Chow, Nano Lett. **16**, 4174 (2016).
[13] T. D. Nguyen, S. Mao, Y. W. Yeh, P. K. Purohit and M. C. McAlpine, Adv. Mater. **25**, 946 (2013).
[14] S. R. Spurgeon, J. D. Sloppy, D. M. Kepaptsoglou, P. V. Balachandran, S. Nejati, J. Karthik, A. R. Damodaran, C. L. Johnson, H. Ambaye, R. Goyette, V. Lauter, Q. M. Ramasse, J. C. Idrobo, K. K. Lau, S. E. Lofland, Jr., J. M. Rondinelli, L. W. Martin and M. L. Taheri, ACS Nano **8**, 894 (2014).
[15] B. Cui, C. Song, H. Mao, H. Wu, F. Li, J. Peng, G. Wang, F. Zeng and F. Pan, Adv. Mater. **27**, 6651 (2015).
[16] C. H. Ahn, J. M. Triscone and J. Mannhart, Nature **424**, 1015 (2003).
[17] J. M. Rondinelli, M. Stengel and N. A. Spaldin, Nat. Nanotechnol. **3**, 46 (2008).
[18] J. Heidler, C. Piamonteze, R. V. Chopdekar, M. A. Uribe-Laverde, A. Alberca, M. Buzzi, A. Uldry, B. Delley, C. Bernhard and F. Nolting, Phys. Rev. B **91**, 024406 (2015).
[19] M. Fiebig, J. Phys. D **38**, R123 (2005).
[20] S. R. Spurgeon, P. V. Balachandran, D. M. Kepaptsoglou, A. R. Damodaran, J. Karthik, S. Nejati, L. Jones, H. Ambaye, V. Lauter, Q. M. Ramasse, K. K. Lau, L. W. Martin, J. M. Rondinelli and M. L. Taheri, Nat. Commun. **6**, 6735 (2015).
[21] T. L. Meyer, A. Herklotz, V. Lauter, J. W. Freeland, J. Nichols, E.-J. Guo, S. Lee, T. Z. Ward, N. Balke, S. V. Kalinin, M. R. Fitzsimmons and H. N. Lee, Phys. Rev. B **94**, 174432 (2016).
[22] X. Hong, A. Posadas and C. H. Ahn, Appl. Phys. Lett. **86**, 142501 (2005).
[23] P. M. Leufke, R. Kruk, R. A. Brand and H. Hahn, Phys. Rev. B **87**, 094416 (2013).
[24] N. Izyumskaya, Y. I. Alivov, S. J. Cho, H. Morkoç, H. Lee and Y. S. Kang, Crit. Rev. Solid State Mater. Sci. **32**, 111 (2007).
[25] A. M. Haghiri-Gosnet and J. P. Renard, J. Phys. D **36**, R127 (2003).
[26] See Supplemental Material at_____for the Ti *L*-edge XMCD, magnetic hysteresis loops at 120 K, XRD reciprocal space mapping results, XRD θ-2θ scans results, out-of-plane PFM results with different thickness of PZT, STEM-ABF images near the LSMO/PZT interface, proposed band diagram at the LSMO/PZT interface, Mn $L_{3,2}$-edge and O *K*-edge EELS spectra, STEM-HAADF and the depth profile of out-of-plane lattice spacing, half-integer diffraction results, dependence of deviation on octahedral tilt angles, and summary of half-integer diffraction peaks of three samples from the experiment and the calculation.
[27] W. Lu, P. Yang, W. D. Song, G. M. Chow and J. S. Chen, Phys. Rev. B **88**, 214115 (2013).
[28] N. A. Pertsev, V. G. Kukhar, H. Kohlstedt and R. Waser, Phys. Rev. B **67**, 054107 (2003).
[29] J. Li, Z. Zhu and F. Lai, J. Phys. Chem. C **114**, 17796 (2010).

[30] M. B. Kelman, L. F. Schloss, P. C. McIntyre, B. C. Hendrix, S. M. Bilodeau and J. F. Roeder, Appl. Phys. Lett. **80**, 1258 (2002).
[31] B. Noheda, J. A. Gonzalo, L. E. Cross, R. Guo, S. E. Park, D. E. Cox and G. Shirane, Phys. Rev. B **61**, 8687 (2000).
[32] G. A. Rossetti, A. G. Khachaturyan, G. Akcay and Y. Ni, J. Appl. Phys. **103**, 114113 (2008).
[33] G. K. Williamson and W. H. Hall, Acta Mater. **1**, 22 (1953).
[34] G. Catalan, B. Noheda, J. McAneney, L. J. Sinnamon and J. M. Gregg, Phys. Rev. B **72**, 020102(R) (2005).
[35] B. C. Jeon, D. Lee, M. H. Lee, S. M. Yang, S. C. Chae, T. K. Song, S. D. Bu, J. S. Chung, J. G. Yoon and T. W. Noh, Adv. Mater. **25**, 5643 (2013).
[36] D. Lee, B. C. Jeon, A. Yoon, Y. J. Shin, M. H. Lee, T. K. Song, S. D. Bu, M. Kim, J. S. Chung, J. G. Yoon and T. W. Noh, Adv. Mater. **26**, 5005 (2014).
[37] R. Guo, L. Shen, H. Wang, Z. Lim, W. Lu, P. Yang, Ariando, A. Gruverman, T. Venkatesan, Y. P. Feng and J. Chen, Adv. Mater. Interfaces **3**, 1600737 (2016).
[38] P. Yu, W. Luo, D. Yi, J. X. Zhang, M. D. Rossell, C. H. Yang, L. You, G. Singh-Bhalla, S. Y. Yang, Q. He, Q. M. Ramasse, R. Erni, L. W. Martin, Y. H. Chu, S. T. Pantelides, S. J. Pennycook and R. Ramesh, Proc. Natl. Acad. Sci. U.S.A. **109**, 9710 (2012).
[39] E. Soergel, J. Phys. D **44**, 464003 (2011).
[40] A. L. Kholkin, S. V. Kalinin, A. Roelofs, and A. Gruverman, Review of Ferroelectric Domain Imaging by Piezoresponse Force Microscopy, Scanning Probe Microscopy, (Springer, New York, 2007), pp. 173
[41] S. V. Kalinin, E. Karapetian and M. Kachanov, Phys. Rev. B **70**, 184101 (2004).
[42] L. Pintilie, C. Ghica, C. M. Teodorescu, I. Pintilie, C. Chirila, I. Pasuk, L. Trupina, L. Hrib, A. G. Boni, N. Georgiana Apostol, L. E. Abramiuc, R. Negrea, M. Stefan and D. Ghica, Sci. Rep. **5**, 14974 (2015).
[43] H. Lu, C. W. Bark, D. Esque de los Ojos, J. Alcala, C. B. Eom, G. Catalan and A. Gruverman, Science **336**, 59 (2012).
[44] P. Zubko, D. J. Jung and J. F. Scott, J. Appl. Phys. **100**, 114112 (2006).
[45] I. P. Pronin, E. Y. Kaptelov, E. A. Tarakanov, L. M. Sorokin, V. P. Afanasjev and A. V. Pankrashkin, Integr. Ferroelectr. **49**, 285 (2002).
[46] V. P. Afanasjev, A. A. Petrov, I. P. Pronin, E. A. Tarakanov, E. J. Kaptelov and J. Graul, J. Phys. Condens. Matter **13**, 8755 (2001).
[47] L. Pintilie, I. Boerasu, M. J. M. Gomes, T. Zhao, R. Ramesh and M. Alexe, J. Appl. Phys. **98**, 124104 (2005).
[48] A. Asamitsu and Y. Tokura, Phys. Rev. B **58**, 47 (1998).
[49] A. K. Tagantsev and G. Gerra, J. Appl. Phys. **100**, 051607 (2006).
[50] D. Li, D. Zheng, J. Gong, W. Zheng, C. Jin and H. Bai, ACS Appl. Mater. Interfaces **9**, 24331 (2017).
[51] J. Chen, Y. Luo, X. Ou, G. Yuan, Y. Wang, Y. Yang, J. Yin and Z. Liu, J. Appl. Phys. **113**, 204105 (2013).
[52] N. Balke, R. Ramesh and P. Yu, ACS Appl. Mater. Interfaces **9**, 39736 (2017).
[53] P. V. Yudin and A. K. Tagantsev, Nanotechnology **24**, 432001 (2013).
[54] H. Chen and S. Ismail-Beigi, Phys. Rev. B **86**, 024433 (2012).
[55] F. Bridges, C. H. Booth, M. Anderson, G. H. Kwei, J. J. Neumeier, J. Snyder, J. Mitchell, J. S. Gardner and E. Brosha, Phys. Rev. B **63**, 214405 (2001).
[56] J. García, M. C. Sánchez, G. Subías and J. Blasco, J. Phys. Condens. Matter **13**, 3229 (2001).
[57] T. Shibata, B. A. Bunker and J. F. Mitchell, Phys. Rev. B **68**, 024103 (2003).
[58] R. F. Egerton, Rep. Prog. Phys. **72**, 016502 (2009).
[59] H. Kurata and C. Colliex, Phys. Rev. B **48**, 2102 (1993).
[60] M. Varela, M. P. Oxley, W. Luo, J. Tao, M. Watanabe, A. R. Lupini, S. T. Pantelides and S. J. Pennycook, Phys. Rev. B **79**, 085117 (2009).
[61] A. M. Glazer, Acta Crystallogr. A **31**, 756 (1975).

[62] A. M. Glazer, Acta Crystallogr. B **28**, 3384 (1972).
[63] P. M. Woodward, Acta Crystallogr. B **53**, 32 (1997).
[64] S. J. May, J. W. Kim, J. M. Rondinelli, E. Karapetrova, N. A. Spaldin, A. Bhattacharya and P. J. Ryan, Phys. Rev. B **82**, 014110 (2010).
[65] B. Zhang, C. J. Sun, P. Yang, W. Lu, B. L. Fisher, T. Venkatesan, S. M. Heald, J. Chen and G. M. Chow, Phys. Rev. B **89**, 195140 (2014).
[66] R. L. Johnson-Wilke, D. Marincel, S. Zhu, M. P. Warusawithana, A. Hatt, J. Sayre, K. T. Delaney, R. Engel-Herbert, C. M. Schlepütz, J. W. Kim, V. Gopalan, N. A. Spaldin, D. G. Schlom, P. J. Ryan and S. Trolier-McKinstry, Phys. Rev. B **88**, 174101 (2013).
[67] B. Zhang, Properties of strain modulated manganite $Pr_{0.67}Sr_{0.33}MnO_3$ thin films. 2014, National University of Singapore
[68] H. Tolentino, M. Medarde, A. Fontaine, F. Baudelet, E. Dartyge, D. Guay and G. Tourillon, Phys. Rev. B **45**, 8091 (1992).
[69] Y. Zhou, X. Guan, H. Zhou, K. Ramadoss, S. Adam, H. Liu, S. Lee, J. Shi, M. Tsuchiya, D. D. Fong and S. Ramanathan, Nature **534**, 231 (2016).
[70] B. Zhang, J. Chen, P. Yang, X. Chi, W. Lin, T. Venkatesan, C. J. Sun, S. M. Heald and G. M. Chow, Sci. Rep. **6**, 19886 (2016).
[71] A. S. Moskvin, A. A. Makhnev, L. V. Nomerovannaya, N. N. Loshkareva and A. M. Balbashov, Phys. Rev. B **82**, 035106 (2010).
[72] T. Kanki, H. Tanaka and T. Kawai, Phys. Rev. B **64**, 224418 (2001).
[73] H. Chen, Q. Qiao, M. S. Marshall, A. B. Georgescu, A. Gulec, P. J. Phillips, R. F. Klie, F. J. Walker, C. H. Ahn and S. Ismail-Beigi, Nano Lett. **14**, 4965 (2014).
[74] M. Hammouri, E. Fohtung and I. Vasiliev, J Phys Condens Matter **28**, 396004 (2016).
[75] J. D. Burton and E. Y. Tsymbal, Phys. Rev. B **80**, 174406 (2009).
[76] Y. Tokura, Science **288**, 462 (2000).
[77] A. Tebano, C. Aruta, S. Sanna, P. G. Medaglia, G. Balestrino, A. A. Sidorenko, R. De Renzi, G. Ghiringhelli, L. Braicovich, V. Bisogni and N. B. Brookes, Phys. Rev. Lett. **100**, 137401 (2008).
[78] J. Nogués and I. K. Schuller, J. Magn. Magn. Mater. **192**, 203 (1999).
[79] X. Ke, M. S. Rzchowski, L. J. Belenky and C. B. Eom, Appl. Phys. Lett. **84**, 5458 (2004).
[80] M. Huijben, P. Yu, L. W. Martin, H. J. Molegraaf, Y. H. Chu, M. B. Holcomb, N. Balke, G. Rijnders and R. Ramesh, Adv. Mater. **25**, 4739 (2013).